Rain Enhancement and Fog Elimination by Seeding with Charged Droplets. Part I: Theory and Numerical Simulations

A. KHAIN, V. ARKHIPOV, AND M. PINSKY

Institute of the Earth Science, The Hebrew University of Jerusalem, Jerusalem, Israel

Y. FELDMAN AND YA. RYABOV

Department of Applied Physics, The Hebrew University of Jerusalem, Jerusalem, Israel

(Manuscript received 27 July 2003, in final form 20 March 2004)

ABSTRACT

A new method of droplet collision acceleration, with the purpose of rain enhancement and fog elimination, is proposed. According to the method, some fraction of the droplets is taken from clouds (or fog) themselves, charged, and then injected back into clouds (or fog). To verify the efficiency of the method, a novel model has been developed, allowing simulation of droplet spectrum evolution by collision in case a certain fraction of the droplets in a droplet spectrum is charged. Simulations of droplet spectra evolution include several steps: (a) The forces arising between charged and neutral droplets, as well as between charged droplets, are calculated as the function of the value of the charges, droplet size, and distance between droplets. It is shown that because of the induction effect, significant attraction forces arise between charged and neutral droplets. (b) The results obtained have been used to calculate the collision efficiencies between charged and neutral, as well between charged droplets. As a result, a ''four dimensional'' table of the collision efficiencies (the collision efficiency is the function of the droplet size and charge) was calculated. The collision efficiencies between charged and neutral droplets turn out to be significantly higher than the pure gravity-induced values. (c) To accomplish these simulations, a novel numerical method of solving the stochastic collision equation has been developed. Cloud droplets are described by a two-dimensional size distribution function in which droplets are characterized by both their mass and charge. (d) This model, with the implemented table of the collision efficiencies, has been used to simulate droplet spectra evolution in clouds and fog in case some fraction of these droplets was charged. Simulations of the effects of seeding by charged droplets have been performed. Evolution of initially narrow droplet size spectra (typical of extremely continental clouds in highly smoky air), in the case of seeding and under natural conditions, has been simulated. It was shown that although a natural droplet spectrum does not develop and no raindrops are formed, the injection of just a small fraction of charged particles rapidly triggered the collision process and lead to raindrop formation a few minutes after the injection. Significant acceleration of raindrop formation has been found in the case of a maritime wide-droplet spectrum. Simulations of fog seeding were conducted using droplet spectra distributions of typical fog. Seeding by charged fog droplets of one or both polarities was simulated. In both cases a significant increase in fog visibility was found. The advantages of the seeding method proposed are discussed.

1. Introduction

Rain enhancement and fog elimination are two main fields of weather modification activities that have attracted researchers' attention for many years. Enhancement of rain is of special importance in countries suffering from water shortage for agriculture and other human activities. Fog elimination is highly necessary, for example, to increase visibility, on roads and runways of airports. On the other hand, a shortage of freshwater in some of the mountainous, desert, semidesert, and coastal regions shapes human thinking about the methods of the utilization of fog as an alternative source of freshwater in these regions.

The necessity of special approaches (i.e., cloud seeding for rain enhancement purposes) is related to the fact that the natural process of collisions in clouds (and fog) begins only when droplet size distributions (DSDs) contain a significant concentration of droplets with radii over 20–25 μm (Pruppacher and Klett 1997). Collision efficiencies of droplets with smaller radii are too small to allow for efficient collisions between small droplets. Because the process of diffusion (condensational) droplet growth is quite slow, the time needed for droplets to reach a size large enough to trigger collisions is often too long. As a result, these small droplets may be transported to the upper troposphere by high vertical veloc-

Corresponding author address: Dr. A. Khain, The Ring Family Department of Atmospheric Sciences, Institute of Earth Sciences, The Hebrew University of Jerusalem Givat Ram, Jerusalem 91904, Israel. E-mail: khain@vms.huji.ac.il

ities in convective clouds and freeze to small ice crystals, spreading over a large area without any contribution to precipitation. This situation is typical, for instance, of deep summertime Texas clouds, where the droplet spectrum remains narrow up to the homogeneous freezing level of −38°C (9.5 km) (Rosenfeld and Woodley 2000; Khain et al. 2001). As a result, deep clouds with cloud tops above 10–12 km do not precipitate, or precipitate only slightly.

Visibility in fog is determined by a high concentration of small droplets (5–10 μm). A decrease in droplet concentration due to collisions (accompanied by the formation of larger droplets with a greater sedimentation velocity) would lead to an increase in visibility (fog elimination). However, the supersaturation value in fog is usually very low, which makes diffusional droplet growth very slow (if at all) and prevents droplet collisions, because the efficiency of collisions between small droplets is negligible.

Thus, the main problem that should be solved by seeding both clouds and fog is the acceleration of the process of droplet collisions.

The main idea of hygroscopic seeding, widely employed at present for weather modification purposes, is to increase the rate of droplet collisions by increasing the concentration (or creation) of large droplets in the DSD. Usually, clouds are seeded by soluble particles, which play the role of cloud condensational nuclei (CCN). It is assumed that the spectrum of seed particles contains large CCN. The droplets grown on these CCN are larger than natural droplets and attain the size needed for collision triggering earlier (and at lower levels) than the other droplets.

The prior art hygroscopic seeding techniques suffer from numerous drawbacks. For example, when granular materials are used as seed agents, their hygroscopic nature often causes agglomeration and caking when in storage, even in the presence of a low moisture content. These negative phenomena lead to the creation of particles of sizes, which are usually much greater than the desired value, that are, for example, about 1–10 μm in radius. Although huge hygroscopic particles could be appropriate for the creation of large drop collectors, such particles are rather heavy for transportation by airplanes to provide the desirable concentration of such particles into clouds.

Another example of hygroscopic materials widely used for cloud seeding is the particles obtained by burning (i.e., flares) (Mather et al. 1996, 1997; Bigg 1997; Silverman and Sukarnjanaset 2000). A randomized experiment of seeding young, growing tropical convective clouds by large hygroscopic particles prior to the formation of the first radar echo has produced evidence of an accelerated collision–coalescence process and showed a statistically significant increase in the raindrop formation rate (Silverman and Sukarnjanaset 2000).

Despite these encouraging results, many unresolved problems still remained (Bruintjes 1999). For instance, according to Woodley and Rosenfeld (1999), apparent rain enhancement may come from the large-particle tail (i.e., giant CCN) of the particulate distribution from the flares. If so, the concentrations of these giant CCN are far below the optimum. There is a risk that such a small concentration of these particles may be conducive only to the formation of isolated large raindrops that produce strong radar echoes but may not lead to rain intensification. This would cause an overestimation of the indicated seeding effect when evaluated with the weather radar using a fixed reflectivity–rain rate relationship (Yin et al. 2001).

Numerical simulations of hygroscopic seeding effects on precipitation, conducted by Reisin et al. (1996), using an axisymmetric spectral microphysics cloud model, and Yin et al. (2000), using a 2D slab-symmetry model, revealed a significant potential for rain enhancement. Segal et al. (2004) used a very precise spectral (bin) microphysics cloud parcel model in numerical simulations of hygroscopic seeding of clouds with commercial flares. They showed that the utilization of typical commercial flares did not lead to any significant acceleration of raindrop formation in ascending cloud parcels. The latter result is explained by the fact that commercial flares contain mainly small particles, leading to the growth of small droplets. Because the effects of small and large particles on the DSD broadening and the formation of large droplets are quite opposite, the total effect of seeding is not clear. In the experiments by Segal et al. (2004), the positive effect of large seed particles is largely compensated by the negative effect of a huge number of small seed CCN (which leads to an increase in the droplet concentration slowing down droplet growth).

The hygroscopic seeding of warm fog aims at the decrease in humidity by absorption of water vapor on large seeding particles. If the mass of seeding salt particles is large enough, the air humidity becomes lower and may lead to the evaporation of the smallest fog droplets (while hygroscopic particles will grow). The efficiency of the method is low because (a) a quite high concentration of large hydroscopic particles should be injected to decrease the concentration of fog droplets by a few percent, and (b) after a short time the water fraction in the hygroscopic particles increases and the competition mechanism becomes inefficient.

Thus, both from the theoretical point of view and because of certain technical difficulties, hydroscopic seeding (at least, at present) does not ''close'' the problem of rain enhancement. The creation of large droplets by hygroscopic seeding with large CCN is not the only way to increase the collision efficiency. Based on the utilization of the ''gravity induced'' mechanism of droplet collisions, this method may not be optimal (and, at least, not exhaustive). It allows one to look for other methods leading to rain enhancement. In this study, we propose a new method of acceleration of droplet collisions aimed at rain enhancement and fog elimination.

Electrostatic effects are known to play an important role in the cloud microphysics (Pruppacher and Klett 1997; Tinsley et al. 2000, 2001). Cloud droplets can be charged by different mechanisms, such as ion diffusion, convection charging, inductive charging, thermoelectric effects, contact potential effects, and so on. (Pruppacher and Klett 1997, p. 811–827). DuBard et al. (1983) managed to charge 1-μm-radius aerosol particles by free electrons to values exceeding more than 10^3 elementary charges. Such a particle charge is close to the maximal one (see below).

Effects of the droplet charge were studied in relation to aerosol scavenging and atmospheric cleaning. Grover and Beard (1975) calculated collision efficiencies between droplets with the radii ranging from 42 to 142 μm and small particles with radii of 0.4 and 4.0 μm. Calculations were conducted both for cases when droplets and particles were assumed to be conducting spheres and for cases when the charges were assumed to be in the center of nonconducting spheres. They found a significant increase in collision efficiency when the droplets were loaded with a charge of the magnitude typical of thunderstorm clouds [$>7 \times 10^4$ elementary (electron) charges], while small particles were charged with charges of the opposite polarity.

Wang et al. (1978) conducted a set of calculations of the collision efficiency between charged aerosol particles and droplets, assuming that (a) colliding particles have the opposite polarity, and (b) attraction between the colliding particles arises due to the attraction of point charges located in the particle center. In the calculations the charges on colliding particles and droplets were assumed to be proportional to the square of their radii, so that the droplet charge was always much greater than the particle charge. In the work cited, the charge of a droplet was thousands of elementary charges and the charge of an aerosol particle was from 1 to more than 40 elementary charges. In this case, a modest increase in the collision rate was found for aerosol particles of radii 0.1–1.0 μm, with droplets of radii of a few tens of microns. The droplet charge used in the simulations was of the same order of magnitude as that produced in thunderstorms. The general conclusion drawn from these and other results was the following: beyond the regions of thunderstorm processes, the effect of electrical forces on particle–droplet collision efficiency for natural clouds is comparatively weak.

Note that this result was obtained for very low charges on aerosol particles, and in neglecting image charge forces (induced charges). These effects were taken into account by Tinsley et al. (2000), who studied the effects of charges on the efficiency of collisions between droplets and aerosol particles under the assumption that charged aerosol particles are formed from evaporating charged droplets at the cloud tops. The authors took into account image charge forces that have been shown to produce a drastic increase in the collision efficiency as compared to that for neutral particles. Collisions were accelerated even in cases in which droplets and aerosol particles were charged with charges of the same polarity. They found that even for nonthunderstorm clouds electrical effects considerably increase the scavenging rate of charged aerosol particles of 0.1–1.0-μm radii. The authors call this process ''electroscavenging.''

Returning to the problem of the artificial increase of the collision efficiency between droplets with the purposes of rain enhancement and fog elimination, we would like to note that it is supposedly not a difficult technical problem as regards charging droplets of clouds and fog with the values that are much higher than those usually observed in natural clouds, and to use these charged droplets as seeding particles. We show that seeding with charged droplets may be a very efficient tool for rain enhancement and fog elimination purposes.

In this paper we consider some theoretical aspects of cloud (and fog) seeding with charged droplets. In section 2 we present and discuss the values of electrostatic forces between charged (as well as charged and neutral) droplets. Section 3 is dedicated to the calculation of collision efficiencies between both charged and neutral droplets. Section 4 describes a novel model solving the stochastic coalescence equation in the case that colliding droplets are characterized both by their mass (as in the classical approach) and by their charge. The results of the simulation of droplet spectrum evolution in clouds and the simulation of visibility in fog under natural and seed conditions are presented in section 5. We summarize the results in section 6. In appendix A we present the approximate solution of the electrostatic force arising between the two charged cloud droplets, and in appendix B we discuss the characteristic time of electrostatic leakage of cloud droplet charge.

2. Electrostatic interaction between two drops

Usually cloud droplets are formed on aerosol particles containing a certain soluble fraction. It means that droplets contain a sufficient number of ions to be regarded as conductive particles.

Previous calculations of electroscavenging (see, e.g., Tinsley et al. 2000, 2001) are related to the electrostatic interaction between a charged aerosol particle (the point charge is located at the particle center) and a droplet charge (charged conductive sphere) (see appendix A). We generalize this approach for the case of two conductive insulated spheres, taking into account the electrostatic interaction between them. This problem has been solved using a general approach of potential and capacitance coefficients corresponding to these spheres (Smythe 1950; Batygin and Toptygin 1978). However, the final formula, which describes the electrostatic force, is represented through the nonlinear combination of the infinite series. It is too complex to be used for numerical modeling. Thus, in appendix A we present an approximated solution of this problem using the method of electrical images. The electrostatic forces of droplet interaction can be represented by the following formula:

$$F_{\text{el}} \approx \frac{Q_1 Q_2}{4\pi\varepsilon_0 R^2} + \frac{1}{4\pi\varepsilon_0}\left\{Q_1^2 r_2\left[\frac{1}{R^3} - \frac{R}{(R^2 - r_2^2)^2}\right] + Q_2^2 r_1\left[\frac{1}{R^3} - \frac{R}{(R^2 - r_1^2)^2}\right] + Q_1 Q_2 r_1 r_2\left[\frac{1}{R^4} + \frac{1}{(R^2 - r_1^2 - r_2^2)^2} - \frac{1}{(R^2 - r_1^2)^2} - \frac{1}{(R^2 - r_2^2)^2}\right]\right\}, \quad (1)$$

where Q_1 and Q_2 are charges of two conductive insulated spheres, r_1 and r_2 are the radii of these spheres, R is the distance between the spheres' centers, and $\varepsilon_0 = 8.854 \times 10^{-12}$ F m^{-1} is the dielectric permittivity of free space. The geometry of droplet interaction and corresponding notations are presented in appendix A (Fig. A3). The first term on the right-hand side of (1) represents the Coulomb force (it decreases with distance as R^2), and the next two terms represent interaction between point charges and the dipole (force decreases as R^3). The last term describes interaction between induced imaginary charges (this force decreases as R^4).

The accuracy of approximation (1) depends on many parameters, for example, charges of the droplets and their radii. However, it is high enough to use this approximation in the study. In more detail, this problem is discussed in appendix A.

Figure 1 shows the dependencies of the electrostatic force between charged droplets of radii $r_1 = 10$ μm and $r_2 = 5$ μm on the distance between the droplets calculated using (1). One can see that the maximum attraction force is obtained when droplets are loaded with charges of the opposite polarity (dotted line in the figure). At the same time, the attraction force between neutral and charged droplets turns out to be significant also (the dash line).

As follows from solution (1), two droplets can attract each other even in the case when they are loaded with charges of the same polarity. This fact can be explained by the effect of imaginary charges. The effect erases at short separation distances (about the sum of the droplet radii) in cases that the droplets' radii (or the magnitudes of droplets' charges) are significantly different. In these cases the attraction force arising between the charge of a droplet and the imaginary charges induced in the counterpart droplet dominates over the Coulomb force's repulsion between the droplets. At the same time, for long separation distances (much bigger than the sum of droplet radii) the Coulomb force always dominates (see the dash–dotted line in Fig. 1). In case the particles are loaded by significant charges of the same polarity, repulsion dominates at all separation distances (solid line in Fig. 1).

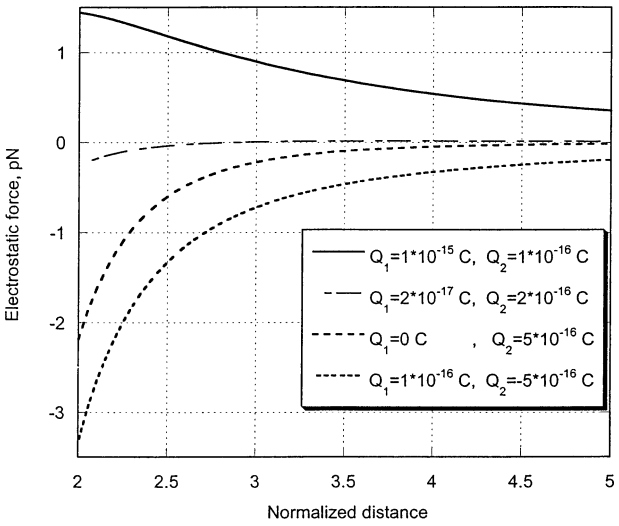

FIG. 1. Electrostatic forces as a function of normalized distance $2R/(r_1 + r_2)$ for different pairs of charges Q_1 and Q_2 according to formula (1): $r_1 = 10$ μm, and $r_2 = 5$ μm.

Theoretically, an insulated particle in the vacuum can be loaded with a charge of an arbitrary large magnitude. However, a cloud droplet situated in the air cannot be charged more than a certain maximum value $Q_{\max}$, which is determined by the air breakdown voltage for the corona discharge $U_b \sim 3 \times 10^6$ V m^{-1} (Meek and Craggs 1953). In appendix B the magnitude of this maximum charge $q_{\max}$ as a quadratic function of the droplet radius was obtained (see Fig. 2). For example, a droplet with radius 1 μm has $q_{\max} = 3.3 \times 10^{-16}$ C and a droplet with radius 10 μm has $q_{\max} = 3.3 \times 10^{-14}$ C.

The corona discharge is not the only process that results in a decrease in the droplet change. Even in the case $Q < q_{\max}$, the charge of a droplet sinks due to the conductivity of air provided by the mobility of free ions in the air. In this case a charged droplet slowly loses its charge according to the exponential law $Q = Q_0 \exp(-t/\tau)$, where $\tau = \varepsilon_0/\sigma$ is the relaxation time, σ is the conductivity of air, and Q_0 is the initial charge of a droplet (Pruppacher and Klett 1997, p. 794). The fair weather sea level conductivity estimated was $\sigma \approx 2.3 \times 10^{-14}$ S m^{-1}, which gives the value of $\tau \approx 6.5$ min. However, the conductivity inside a cloud is significantly lower than the fair weather sea level conductivity, because the concentration of free ions inside a cloud is significantly lower than that in the cloud-free air. Pruppacher and Klett (1997, p. 802) estimate the conductivity inside a cloud in the interval from 1/40 up to 1/3 of the fair weather sea level conductivity, which leads to values of relaxation time τ from 20 min up to 4 h. Similar estimations of τ are presented by Tinsley et al. (2000). It means that the time period of the droplet discharge is much longer than the time scale of the

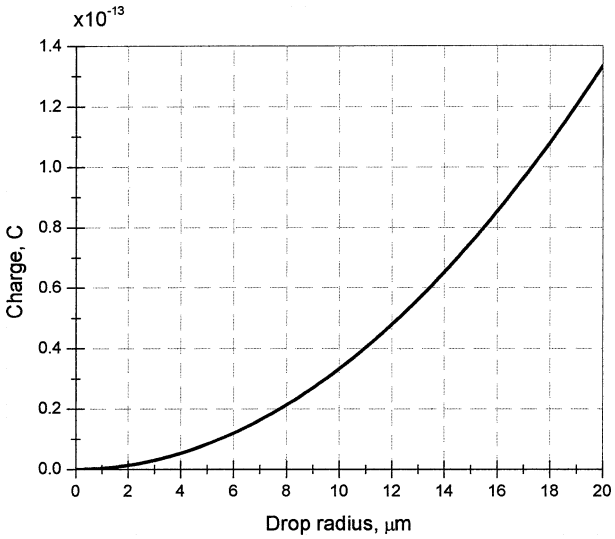

FIG. 2. Maximum charge that a drop can be loaded as a function of drop radius.

coagulation processes leading to raindrop formation, which are typically about 10 min for cumulus clouds. Thus, our simulation of the coagulation process will be conducted under the assumption of charge conservation.

3. Calculation of the collision efficiencies

The rate of drop collisions is determined by the collision efficiency defined as the ratio of the collision cross section S_c to the geometrical cross section $S_g = \pi(r_1 + r_2)^2$ (Fig. 3). In the case of pure gravity collisions, the collision efficiency between small cloud droplets is usually much lower than unity (Pinsky et al. 2001). In the case in which the drop collector is charged, the collision cross section increases significantly, so that the collision efficiency can easily exceed unity (right-hand side Fig. 3).

Calculation of the collision efficiencies is a complicated problem of the hydrodynamic interaction between two drops moving in an airflow. In our work we use the superposition method (Pruppacher and Klett 1997). This method assumes that each drop moves in a flow field induced by its counterpart moving alone. Dating back to Langmuir (1948), this method has been successfully used by many investigators (e.g., Shafrir and Gal-Chen 1971; Lin and Lee 1975; Schlamp et al. 1976; Pinsky et al. 2001) in a wide range of droplet Reynolds numbers. It is known that the precision of the superposition method decreases in cases where colliding droplets are of a similar size and the time of the hydrodynamic interaction increases (see, e.g., Pinsky et al. 1999). Note that, because the electric forces tend to increase the attraction between charged and neutral droplets, the time of interaction in the charge calculations is less than that in the case of neutral droplet collisions. We believe, therefore, that in cases in which the method works for collisions of neutral droplets, it also has to work well in charge calculations.

According to the superposition method, the equation of motion (in a stagnant frame) of drop 1 during its hydrodynamic interaction with drop 2 can be written as

$$\frac{d\mathbf{V}_1}{dt} = -\frac{1}{\tau_1}(\mathbf{V}_1 - \mathbf{V}_{1t}\mathbf{e}_z - \mathbf{u}_2) \quad \text{and} \tag{2}$$

$$\frac{d\mathbf{x}_1}{dt} = \mathbf{V}_1, \tag{3}$$

where $\mathbf{x}_1$ is the vector of the drop 1 coordinate, $\mathbf{V}_1$ is the velocity of drop 1, V_{1t} is the terminal velocity of drop 1 in calm air, $\mathbf{e}_z$ is the unit vector directed downward, $\tau_1 = V_{1t}/g$ is the characteristic relaxation time of drop 1, which is the measure of the inertia, and $g = 9.8$ m s^{-2} is the acceleration of gravity. In the present study we will conduct our simulations for small drops ($r \leq 20$ μm) with small Reynolds numbers (Re ≤ 0.1). For such Stokesian droplets

$$\tau_1 = \frac{2}{9}\frac{\rho_w}{\eta}r_1^2, \tag{4}$$

where r_1 is the radius of drop 1, $\rho_w = 1000$ kg m^{-3} is water density, and $\eta = 1.8 \times 10^{-5}$ kg m s^{-1} is dynamic air viscosity. In (2) $V_{1t}\mathbf{e}_z/\tau_1$ is the acceleration of drop 1 induced by gravity, and $\mathbf{u}_2$ is the perturbed velocity induced by drop 2 at the location of the drop 1 center, and so $\mathbf{u}_2/\tau_1$ is the acceleration of drop 1 caused by the perturbations of air velocity induced by drop 2.

According to the superposition method, the perturbed velocity fields induced by drops are calculated under the assumption that the droplets move independently. For each drop, the value and direction of the induced velocity are determined by the current relative drop velocity with respect to air. The components of velocity $\mathbf{u}_2$ depend on the drop–air relative velocity of drop 2, $\mathbf{U}_2$, the separation distance R between the droplets, and the radius of drop 2. That is,

$$\mathbf{u}_2 = \mathbf{u}_2(\mathbf{U}_2, R, r_2), \tag{5}$$

where

$$\mathbf{U}_2 = \mathbf{V}_2 - \mathbf{u}_1. \tag{6}$$

For small Reynolds numbers the flow induced by moving spheres obeys the Stokes solution (Kim and Karrila 1991, p. 90) with the radial u_{2r} and normal $u_{2\alpha}$ components of velocity represented in the spherical coordinate frame connected with drop 2 as

$$u_{2r} = |U_2|\cos\alpha_2\left[\frac{3}{2}\frac{r_2}{R} - \frac{1}{2}\left(\frac{r_2}{R}\right)^3\right] \quad \text{and}$$

$$u_{2\alpha} = -|U_2|\sin\alpha_2\left[\frac{3}{4}\frac{r_2}{R} - \frac{1}{4}\left(\frac{r_2}{R}\right)^3\right], \tag{7}$$

where α_2 is the angle between the drop–air relative velocity of drop 2 and the straight line connecting the

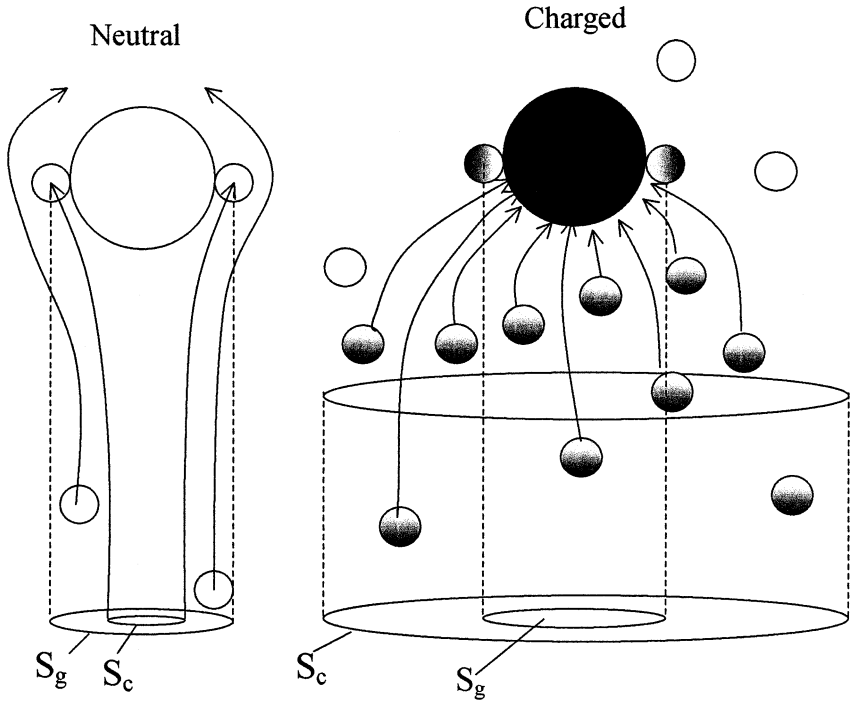

FIG. 3. Scheme of hydrodynamic droplet interaction and collisions in the cases of (left) neutral droplets and (right) charged drop collector. In the case of neutral droplet collisions, the collision cross section S_c is less than the geometrical cross section S_g (the collision efficiency $E = S_o/S_g < 1$). In the case in which the drop collector is charged, $E = S_o/S_g > 1$.

centers of interacting drops. The induced velocity tends to be zero, with an increase of the separation distance between droplets; so, if $R \to \infty$ then $u_{2r} \to 0$ and $u_{2\alpha} \to 0$.

Equations of motion for drop 2 are analogous and can be obtained from (2)–(7), replacing index 1 by 2.

In the case of charged droplets, the electrostatic force $\mathbf{F}_{el}$ should be added to the droplet motion (2),

$$\frac{d\mathbf{V}_1}{dt} = -\frac{1}{\tau_1}(\mathbf{V}_1 - \mathbf{V}_{1t}\mathbf{e}_z - \mathbf{u}_2) + \frac{\mathbf{F}_{el}}{m_1},$$

$$\frac{d\mathbf{x}_1}{dt} = \mathbf{V}_1,$$

$$\frac{d\mathbf{V}_2}{dt} = -\frac{1}{\tau_2}(\mathbf{V}_2 - \mathbf{V}_{2t}\mathbf{e}_z - \mathbf{u}_1) - \frac{\mathbf{F}_{el}}{m_2}, \quad \text{and}$$

$$\frac{d\mathbf{x}_2}{dt} = \mathbf{V}_2, \tag{8}$$

where m_1 and m_2 are the masses of droplets. It should be noted that the magnitude of the electrostatic force in (8) is determined by expression (1), while the direction of this force is parallel to the line connecting the drop centers. In the first line in (8), $\mathbf{F}_{el}$ is opposite to the force in the third line of these equations because of the third Newtonian law.

To illustrate a comparable role of the electrostatic forces (represented by the term $\mathbf{F}_{el}/m_1$) and the hydrodynamic forces during the hydrodynamic interaction [represented by the term $(-\mathbf{u}_2/\tau_1)$] of charged and neutral droplets, the radial component of the difference between these forces was calculated as the function of the distance between surfaces of the 10-μm-radius charged droplet and 5-μm-radius neutral droplet (Fig. 4). The charge of the 10-μm-radius droplet varied from 5% to 100% of the maximum value. For the sake of convenience, the comparison with the case of interaction of neutral droplets is presented as well. The initial location of the droplets is chosen in such a way that in case the droplets are neutral, no collision takes place. In the figure, the forces are normalized by the weight of the 5-μm-radius droplets. One can see that at larger distances the repulsion force (positive values) caused by the droplet hydrodynamic interaction dominates. It means that the hydrodynamic interaction force exceeds the electrostatic force. In the case in which the droplets are neutral, the repulsion force prevents the droplet collision. In the figure it can be seen by the existence of the minimal distance between the droplet surfaces (of about 1.7 μm). If the 10-μm-radius drop is loaded even by a small charge, the droplet interaction changes dramatically; at smaller distances (whose magnitude depends on the droplet charge) the attraction force dominates and can exceed the force of hydrodynamic interaction (as well as the gravity force) by 1000 and more times. So, when droplets are approaching at distances so small that the

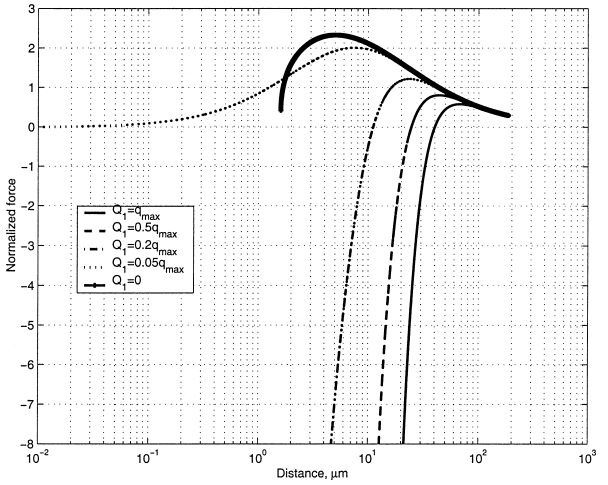

FIG. 4. The radial forces affecting the motion of 10-μm-radius and 5-μm-radius droplets during their approaching. The forces are calculated for different charges of the 10-μm-radius droplet. The magnitude of the forces is normalized by the weight of the 5-μm-radius droplet. Positive values of the forces foster the drop repulsion; the negative forces foster the droplet attraction. The electrostatic attraction force dominates over the hydrodynamic repulsion force within a wide range of droplet separation distances.

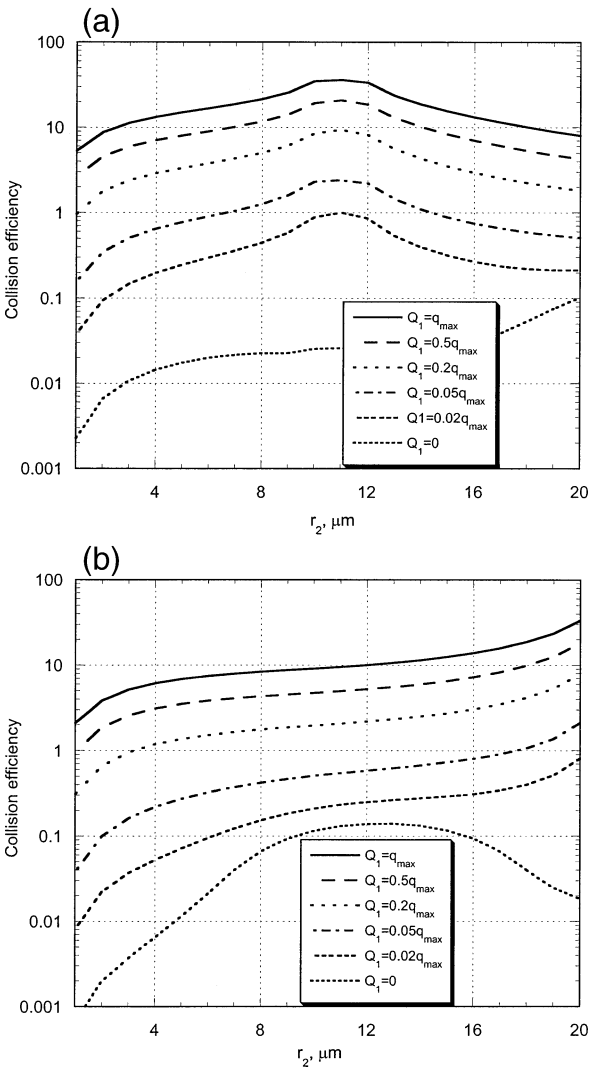

FIG. 5. (a) Collision efficiencies between a charged 10-μm-radius droplet and neutral cloud droplets with radii ranged from 1 to 20 μm. The charge of the 10-μm-radius drop varies from zero to the maximum possible value. (b) The same as in (a), but for a charged 20-μm-radius droplet.

huge attraction force fully determines the droplet behavior, one can expect the droplet collision.

Equation (8) was used for collision efficiency calculations. For this purpose, we used a procedure similar to that developed by Pinsky et al. (1999, 2001). Initially, interacting droplets were located at large separation distances (30 radii of the largest droplet in a drop pair). At this distance the velocity fields $\mathbf{u}_1$ and $\mathbf{u}_2$ as well as the electrical forces $\mathbf{F}_{el}$ were equal to zero; hence, drop velocities were equal to terminal velocities. By varying the initial location of the smaller droplet in the direction perpendicular to the direction of gravity force, the grazing trajectories and the effective collision cross section S_c were determined (see Fig. 3). The equation system (8) was solved using the fifth-order Runge–Kutta method, with automatic precision control and automatic choice of the integration time step (Press et al. 1992).

Using this procedure, a four-dimensional (with respect to droplet sizes and charges) table of the collision efficiency has been calculated. The collision efficiencies calculated are the result of the contribution of two forces: the electrostatic force and gravity. As a result, the collision efficiency can be either larger or smaller than the pure gravity value. Note, however, that in the majority of cases the electrostatic forces lead to a dramatic increase in the collision efficiency values. It means that the total effect must be a crucial increase in the collision rate in a droplet population containing charged droplets.

Figures 5a and 5b present the collision efficiencies between charged drops of the 10- and 20-μm radii, respectively, and neutral cloud droplets with radii ranged from 1 to 20 μm. Figure 6 shows the collision efficiencies between drops of different radii charged with their maximum possible charge and neutral droplets. Figure 7 presents the collision efficiencies between droplets charged with the maximum possible charge (droplet radii of these droplets are plotted along the y axis) and the droplets charged with the charge of the opposite polarity and equal to 5% of the maximum value. The collision efficiencies highly depend on droplet charge and size. In the case of charge-neutral droplet collisions, the collision efficiencies may reach 20–30; that is, the values are several hundred times the gravity-induced values. In the case in which droplets are charged by opposite polarities (Fig. 7), the collision efficiencies may reach a few thousand, that is, $\sim 10^4$ times the gravity-induced values. We see that in cases in which droplet charges are not negligibly small, the attraction forces

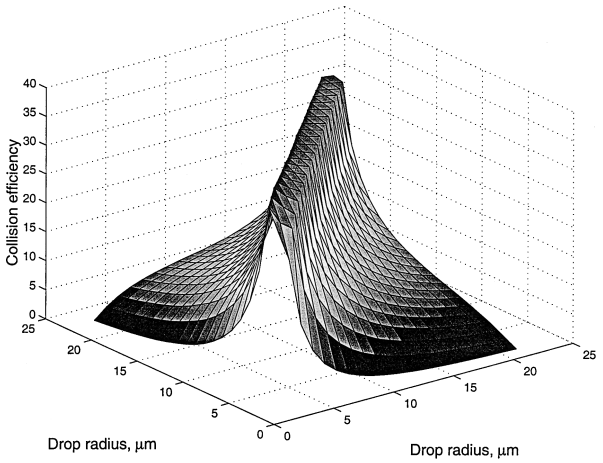

FIG. 6. Collision efficiencies between drops of different radii charged with their maximum possible charge (the *x* axis) and neutral droplets (the *y* axis).

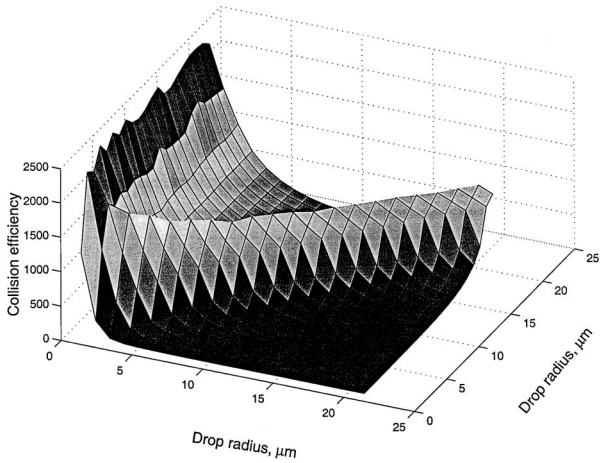

FIG. 7. Collision efficiencies between droplets charged with the maximum possible charge (the *y* axis) and the droplets charged with the charge of the opposite polarity and equal to 5% of the maximum value (the *x* axis).

significantly exceed the forces of the hydrodynamic interaction at small separation distances. So, when droplets approach at such small distances, where attraction force fully determines the droplet behavior, one can expect droplet collision.

It means that charged drop collectors can collect droplets within a volume with the cross section S_c, which significantly exceeds the geometrical cross section S_g. Note that in our calculations below we do not take into account collisions between droplets of the same size. At the same time such collisions can take place in the cases that droplets are charged. Therefore, we suppose that the values of the collision rate obtained in the calculations presented are somewhat underestimated.

4. Modeling of stochastic collisions

Numerical modeling of clouds requires simulation of various processes such as cloud droplet nucleation, their diffusion growth, and the evolution of a raindrop spectrum. One of the most important mechanisms of raindrop formation is the collision of cloud droplets. The process of the droplet spectrum formation by drop–drop collisions is described by a well-known stochastic collision equation (SCE) (Pruppacher and Klett 1997):

$$\frac{\partial f(m, t)}{\partial t} = \int_0^{m/2} f(m_c, t)K(m_c, m')f(m', t)\, dm' - \int_0^{\infty} f(m, t)K(m, m')f(m', t)\, dm', \quad (9)$$

where $f(m, t)$ is the DSD at time t and $K(m_c, m')$ is the collection kernel describing the rate at which a drop of mass $m_c = m - m'$ is collected by a drop of mass m', forming further a drop of mass m. The first integral on the right-hand side of (9) (the so-called gain) describes the gain of drops of mass m by collision and coalescence of two smaller drops, while the second integral (loss integral) denotes the loss of drops with mass m due to collisions with other drops of any size.

Many different methods have been developed for the numerical solution of the SCE (Kovetz and Olund 1969; Bleck 1970; Berry and Reinhardt 1974; Tzivion et al. 1987; Seeßelberg et al. 1996; Bott 1998; Khain et al. 2000). In our case the problem of droplet collisions is more complicated than the problem of the purely gravitational collisions, because now the collection kernel must depend on droplet charges. The distribution function for water droplets becomes two-dimensional: in each mass category there are droplets with different charges. Thus, an additional grid corresponding to droplet charges was introduced. As a result, we have introduced a logarithmically equidistant two-dimensional mass charge grid. This grid contains 1000 mass bins describing droplet size distribution with droplet radii ranging from 1 up to 2000 μm, and 35 charge bins with charges ranging from -2×10^{-13} up to 2×10^{-13} C. When calculating the collisions, we take into account the maximum charge constraint (see Fig. 2 and appendix B).

Within the mass grid two ranges of droplet sizes were considered: droplets with radii equal to or below 21 μm and droplets with radii exceeding 21 μm. Numerical evaluations show that if originally charged droplets are comparatively small (say below 15 μm), the effect of a droplet charge on collisions significantly decreases when the radius of the larger droplet in the pair exceeds 21 μm (as a result of collisions). Thus, for such droplets we neglect the electrostatic effects. This assumption, most probably, leads to some underestimation of the collision rate.

In our model we considered three different types of collisions for two droplets. The first: the radii of both colliding droplets are less than 21 μm, and the radius

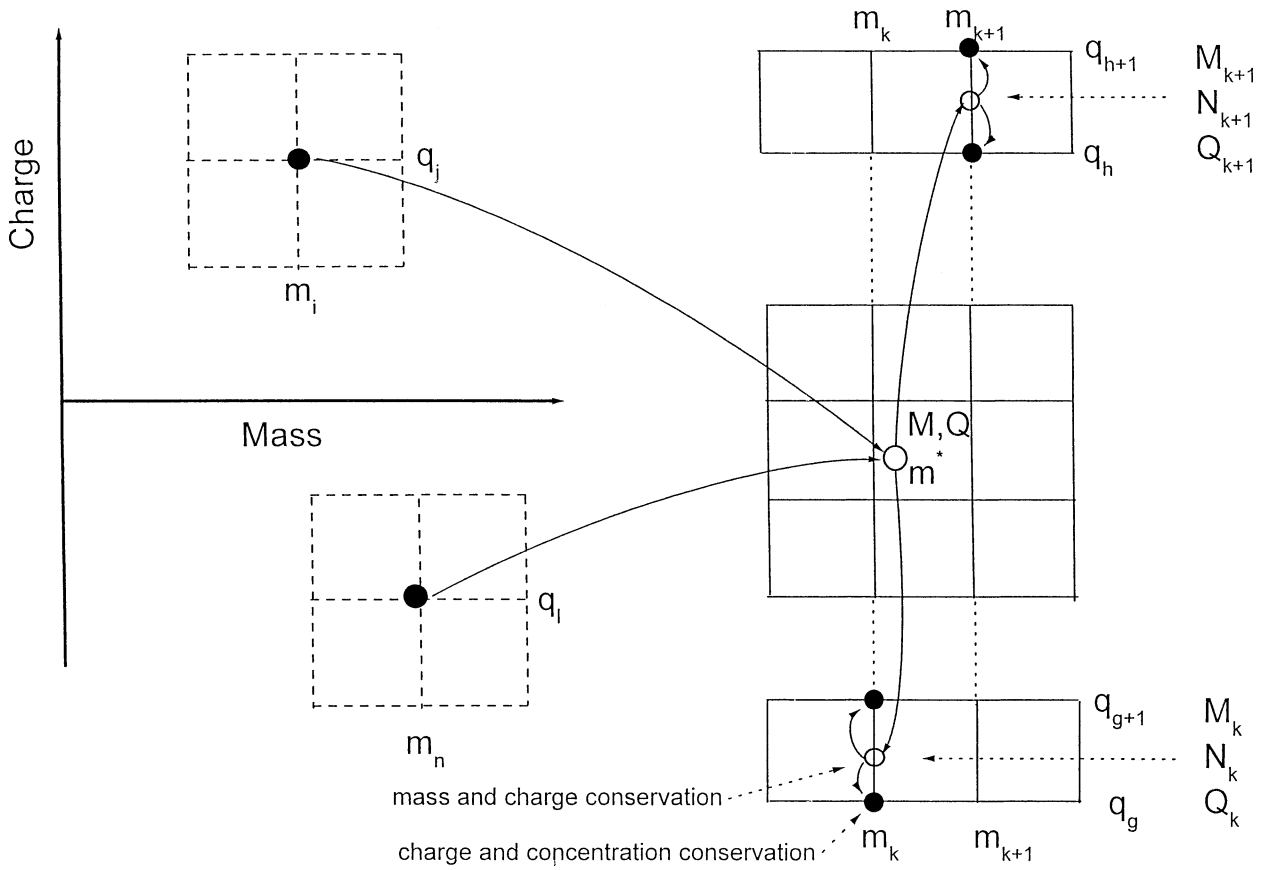

FIG. 8. Scheme of remapping of drop mass and charges on regular mass and charge grids in the case of collisions of charged droplets.

of the droplet created after collision is below 21 μm. In this case both the gain integral and the loss integral are calculated using the entire two-dimensional size charge distribution. The second: the radii of colliding droplets are below 21 μm, but the droplet obtained as a result of collision is larger than 21 μm. In this case the loss integral is calculated using the entire two-dimensional size charge distribution, while the gain integral is obtained with reduced one-dimensional DSD depending only on droplet masses. The third: at least one droplet in the colliding pair exceeds 21 μm. In this case both the gain and the loss integrals are calculated using the reduced one-dimensional DSD. This approach also leads to some underestimation of the collision rate.

Because the masses (and charges) of the droplets formed by collisions do not coincide with the nodes of the regular grid, a remapping of created droplets into the regular mass and charge meshes is required. The procedure of remapping consists of two steps: remapping of the mass and remapping of charges.

To illustrate the remapping procedure employed, let us consider collisions between the droplets of two categories: a bin of droplets with mass m_i and charge q_j and a bin of droplets with mass m_n and charge q_l (Fig. 8). As a result the collisions between these droplets with mass $m^* = m_i + m_n$ are created, and the corresponding bins lose the mass M and charge Q. If the mass of the resulting drops is located between two categories of a regular mass grid $m_k \le m^* \le m_{k+1}$, the total mass of these droplets is initially added to the kth category. At the first step, according to the procedure proposed by Bott (1998), a certain fraction of mass M is transported from category k to category $k + 1$. As a result, we obtain the additional masses M_k and M_{k+1}, which are added to kth and $(k + 1)$th categories. The additional droplet concentrations N_k and N_{k+1},

$$N_k = \frac{M_k}{m_k} \quad \text{and} \quad N_{k+1} = \frac{M_{k+1}}{m_{k+1}}, \tag{10}$$

are also added to categories k and $k + 1$.

The second step is the redistribution of charge Q. Initially one must redistribute charge Q between the kth and $(k + 1)$ mass categories. We assumed that the distribution of charges between these categories is proportional to the distribution of masses M_k and M_{k+1},

$$Q_k = \frac{M_k}{M_k + M_{k+1}} Q \quad \text{and} \quad Q_{k+1} = \frac{M_{k+1}}{M_k + M_{k+1}} Q, \tag{11}$$

which provides charge conservation. Then, we must redistribute the charges Q_k and Q_{k+1}, added to kth and $(k + 1)$th mass categories, onto the charge grid within the

mass categories. Let us introduce averaged charges of single droplets Q_k/N_k and Q_{k+1}/N_{k+1} related to the kth and $(k + 1)$th mass categories. These averaged charges must correspond to certain cells of the charge grid defined by the inequalities (see Fig. 8)

$$q_g \le \frac{Q_k}{N_k} < q_{g+1} \quad \text{and} \quad q_h \le \frac{Q_{k+1}}{N_{k+1}} < q_{h+1}. \quad (12)$$

To redistribute these averaged charges between the categories of the regular charge grid two conservation conditions must be satisfied: the charge conservation condition and the concentration conservation condition. The charge conservation gives

$$Q_k = N_{k,g}q_g + N_{k,g+1}q_{g+1} \quad \text{and}$$
$$Q_{k+1} = N_{k+1,h}q_h + N_{k+1,h+1}q_{h+1}, \quad (13)$$

where $N_{k,g}$, $N_{k,g+1}$, $N_{k+1,h}$, and $N_{k+1,h+1}$ are concentrations to be added to the bins corresponding to the regular grid charges q_g, q_{g+1}, q_h, and q_{h+1}, respectively. The concentration conservation gives

$$N_{k,g} + N_{k,g+1} = N_k \quad \text{and}$$
$$N_{k+1,h} + N_{k+1,h+1} = N_{k+1}. \quad (14)$$

Then, from (13) and (14) one can finally obtain

$$N_{k,g} = -\frac{Q_k - N_k q_{g+1}}{q_{g+1} - q_g},$$
$$N_{k,g+1} = \frac{Q_k - N_k q_g}{q_{g+1} - q_g}, \quad (15)$$
$$N_{k+1,h} = -\frac{Q_{k+1} - N_{k+1} q_{h+1}}{q_{h+1} - q_h}, \quad \text{and}$$
$$N_{k+1,h+1} = \frac{Q_{k+1} - N_{k+1} q_h}{q_{h+1} - q_h}. \quad (16)$$

Thus, as a result of the remapping, droplets were redistributed into four categories numerated by four pairs of indices (k, g), $(k, g + 1)$, $(k + 1, h)$, and $(k + 1, h + 1)$, where the first index numerates the mass category and the last index numerates the charge category. This remapping procedure provides conservation of the mass and charge, including the charge polarity. It is also worth noting here that the indices of the charge categories g and h, in contrast to the indices of the mass categories k and $k + 1$, are not necessarily neighboring numbers. The reason of this fact is the following: the steps of the mass and charges grids are quite arbitrary, which leads to inequalities (12).

It is important to note here that the remapping procedure provides charge conservation, but the total relevant charge of the system may be inconstant due to two reasons. The first reason is that the charge of droplets obtained as the result of remapping may exceed the value of the maximum possible charge for a droplet of such size. In this situation we assume that the exceeding charge is lost due to the corona discharge and the reduction of the charge of such droplets to the maximum value $q_{\max}$ (see appendix B). The second reason is our assumption that the electrostatic forces are negligible for droplets with the radii exceeding 21 μm. The electrical charge of these droplets is also assumed to be lost.

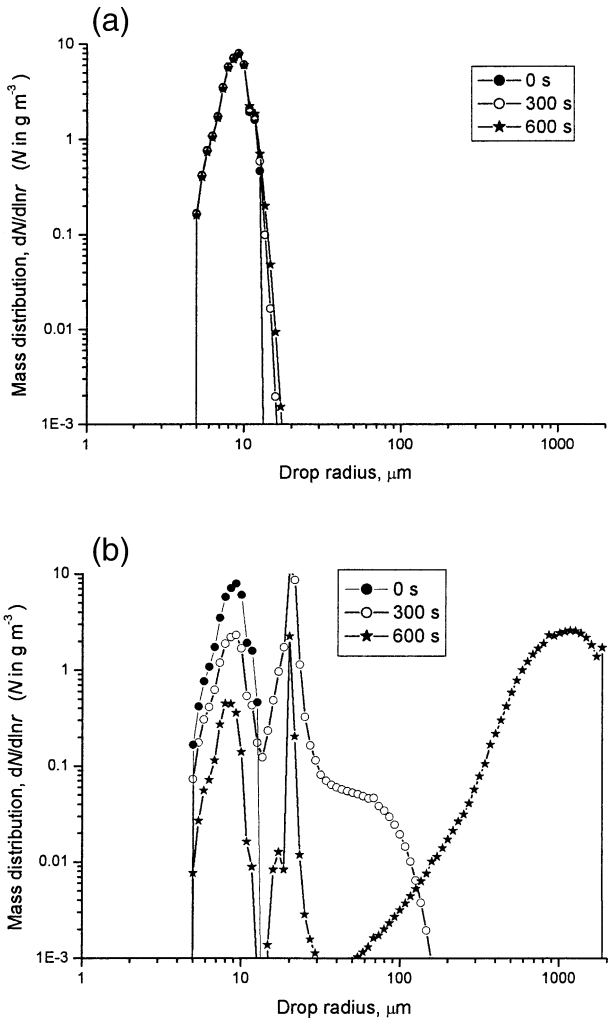

FIG. 9. Continental-type droplet mass distributions at $t = 0$, $t = 300$, and $t = 600$ in cases (a) of noncharged cloud drops and (b) in which 5% of the droplets are charged.

5. Results of seeding simulations

a. Cloud seeding modeling

We employed the procedure described above to investigate the impact of a droplet charge on the coagulation process in clouds. For this purpose we used the droplet mass distribution corresponding to an initially narrow DSD centered at $r = 9$ μm (see the filled-circles curve in Fig. 9) with the total cloud water content of 3 g m^{-3} and droplet concentration of 1100 cm^{-3}. This spectrum is similar to that observed in deep continental

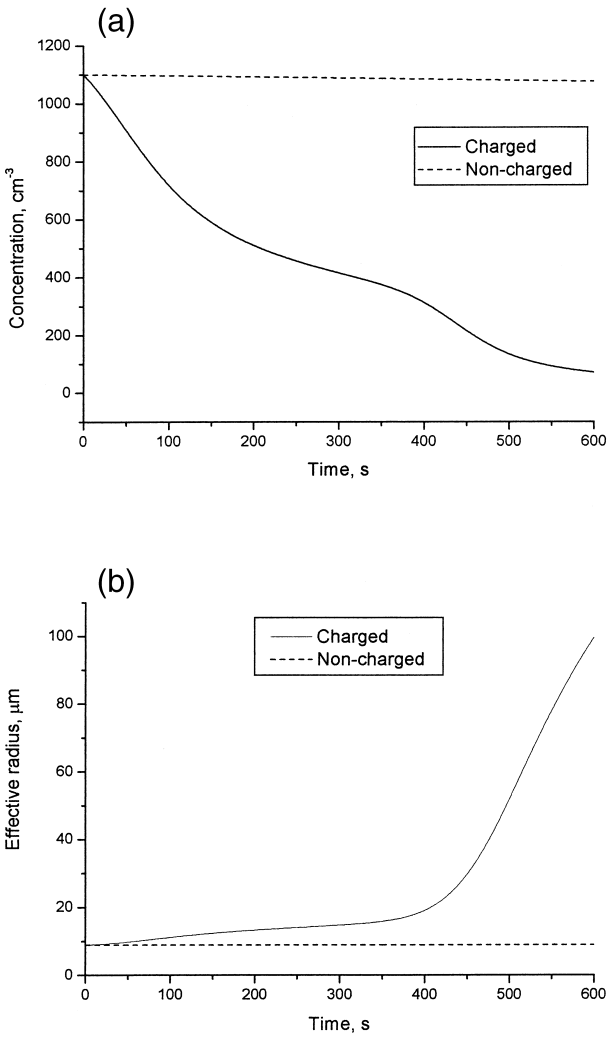

FIG. 10. (a) Time dependence of cloud drops concentration: non-charged cloud (crosses), and for cloud population in which 5% of droplets are charged with maximum charge (open circles). (b) The same as in (a) but for the effective drop radius.

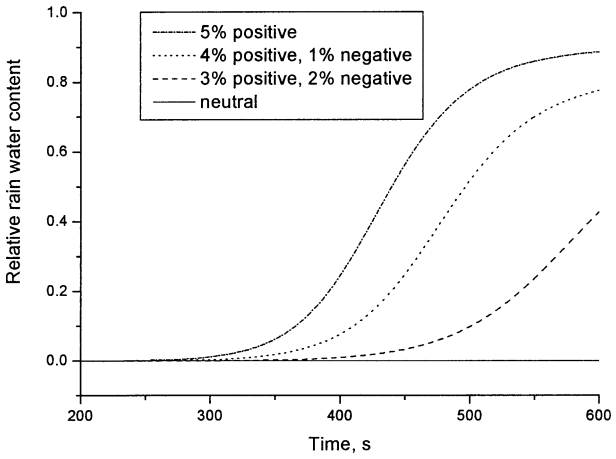

FIG. 11. Time dependence of relative rainwater content for different fraction of negatively and positively charged droplets in droplet population: 5% of charged droplets with positive polarity (dash–dotted curve), 4% of positively charged droplets and 1% of negatively charged droplets (dotted curve), 3% of positively charged droplets and 2% negatively charged droplets (dashed curve), and all droplets are neutral (solid line).

clouds by Rosenfeld and Woodley (2000) in smoky air. The observations and numerical simulations provided by Khain et al. (2001) show that such clouds do not precipitate.

In Fig. 9 one may compare the evolution of the droplets' mass distribution for the neutral (natural) droplets (Fig. 9a) and the evolution of droplets' mass distribution for the case in which 5% of droplets in the initial DSD were charged up to the maximum possible charge q_{max} (see Fig. 2 and appendix B) (Fig. 9b). We also assumed that because of turbulent mixing, all charged droplets are distributed homogeneously within a certain cloud volume, where collisions are simulated. These figures show a crucial influence of droplet charges on the coagulation process. For the charged DSD after 5 min of evolution the droplet mass distribution demonstrates a pronounced tail corresponding to small 50–100-μm raindrops (curve with open circles), which 5 min later develop into 1-mm-radius mature raindrops (curve marked by stars). On the contrary, the neutral DSD in Fig. 9a practically does not develop over the same time period.

Figures 10a and 10b present time dependence of the droplet concentration and the effective radius, respectively. One can see that collisions in a natural cloud are not efficient; hence, droplet concentration and the effective radius do not change with time. By contrast, in the case of ''seeding'' by charged droplets, the concentration of droplets decreases and the effective radius increases drastically during the first 6–7 min of the collision process. The effective radius exceeds 15 μm in the 4 min after seeding. As is known from observations (Rosenfeld and Gutman 1994) and from numerical simulations (Pinsky and Khain 2002), precipitation starts when the effective radius exceeds 15 μm.

To investigate the sensitivity of the coagulation process to the magnitude and polarity of seeding charges, four numerical experiments were conducted (see Fig. 11) in which (a) 5% of charged droplets were assumed to be charged with positive polarity and the rest of the droplets were assumed to be neutral, (b) 4% of positively charged droplets and 1% of negatively charged droplets were assumed, (c) 3% of positively charged droplets and 2% negatively charged droplets were assumed, and (d) all droplets were assumed to be neutral.

The results presented in Fig. 11 (dash–dotted line) show that in the case of 5% of charged droplets almost all cloud water content converted into the rain. This finding is drastically different from the situation of natural (neutral) DSD, which does not lead to the precipitation at all (Rosenfeld and Woodley 2000).

The results presented in Fig. 11 also show that a

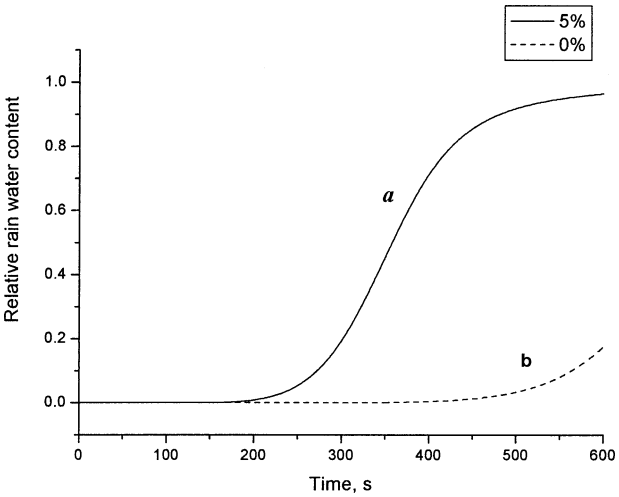

FIG. 12. Time dependencies of the relative rainwater content in the maritime-type droplet mass spectra in cases in which (a) 5% of the droplets were initially charged by their maximal charges and (b) all droplets are neutral.

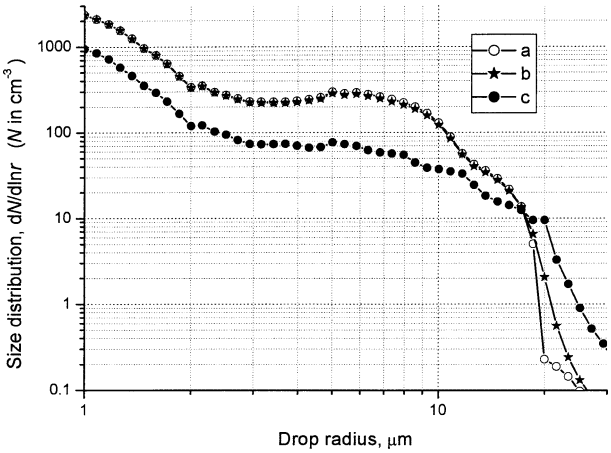

FIG. 13. Droplet size distribution in charged and noncharged fog: $t = 0$ (open circles), 30% fraction of droplets is charged and $t =$ 1800 s (filled circles), and neutral fog, $t = 1800$ s (stars).

unipolar-charged cloud develops faster and precipitates more effectively than a bipolar one. This fact could be explained by the effect of charge compensation. In the case of the bipolar charge, the intensive collisions at the initial stages of coagulation lead to a rapid decrease in the net cloud charge and, consequently, to a decrease in the net effect of the charge on the coagulation. Unipolar charges do not disappear by collisions, and their effect continues during the whole coagulation time.

To verify the ability of the charged droplets to accelerate the raindrop formation in the case of a maritime-type droplet spectrum, we performed an additional simulation, in which 5% of droplets of a maritime-type droplet spectrum centered at ~14 μm (with droplet concentration of ~290 cm^{-3} and cloud water content of 2.9 g m^{-3}) were charged with their maximum possible charges. Figure 12 shows time dependencies of the relative rainwater content in cases in which 5% of the droplets of the maritime DSD are initially charged, as well as for the case of natural DSD development. One can see that the all cloud water converts into rainwater in 6–7 min, that is, even faster than in the case of the continental spectrum. The formation of raindrops under natural conditions begins in ~10 min.

b. Simulations of fog seeding

The problem of fog elimination is actually the problem of increase the visibility (VIS) in fog. The quantitative measure of the visibility is related to the extinction coefficient β by the well-known formula (Zuev 1974)

$$\text{VIS} = -\frac{\ln\varepsilon}{\beta}, \tag{17}$$

where ε is the threshold of contrast, normally equal to 0.02 (Kunkel 1984). If the DSD is known then, assuming a spherical droplet shape, one can estimate the extinction coefficient β as follows:

$$\beta = \int_0^\infty \pi r^2 K(\rho) f(r)\, dr, \quad \text{where}$$

$$K(\rho) = 2 - \frac{8n^2 \sin[2\rho(n-1)]}{\rho(n+1)^2(n-1)},$$

$$\rho = \frac{2\pi r}{\lambda}, \tag{18}$$

r is the radius of a droplet, $f(r)$ is the DSD function for fog, $n = 1.33$ is the refractive index of water, and λ is the wavelength of scattered light (Zuev 1974). In our calculations of the charged seeding effect of the visibility in fogs we used $\lambda = 500$ nm (green light) because this wavelength corresponds to the center of the visible spectrum.

Initially the DSD for fog simulation was chosen to be similar to the DSD of natural fog measured by Roach et al. (1976) (open circles in Fig. 13). This DSD is typical of a fog with the total liquid water content of 0.2 g m^{-3} and droplet concentration of 1400 cm^{-3}. Figure 13 shows the development of the DSD in a natural fog with neutral droplets (the curve marked by stars in Fig. 13) and a fog in which 30% of the droplets were charged positively and another 30% of the droplets were charged negatively (the curve marked by filled circles in Fig. 13). One can see a significant decrease in the concentration of droplets within the 5–10-μm size range after the 30 min of fog development in the case in which the initial DSD contains a fraction of charged droplets mentioned. On the contrary, in the case of natural (neutral) fog the droplet concentration in the 5–10-μm-radii range practically does not change with time. This decrease in the concentration of 5–10-μm droplets leads to a significant increase in visibility as presented in Fig.

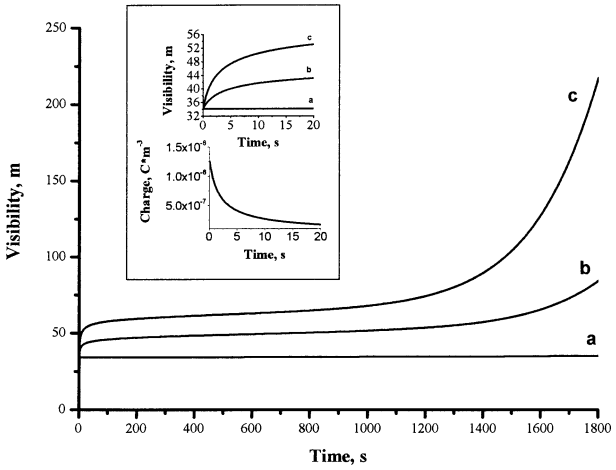

FIG. 14. Time evolution of the visibility in a typical fog for different concentrations of positive and negative charges: (a) neutral, (b) 30% positive, 30% negative, and (c) 50% positive, 50% negative. Framed figure shows the beginning stage of the fog evolution and charge elimination.

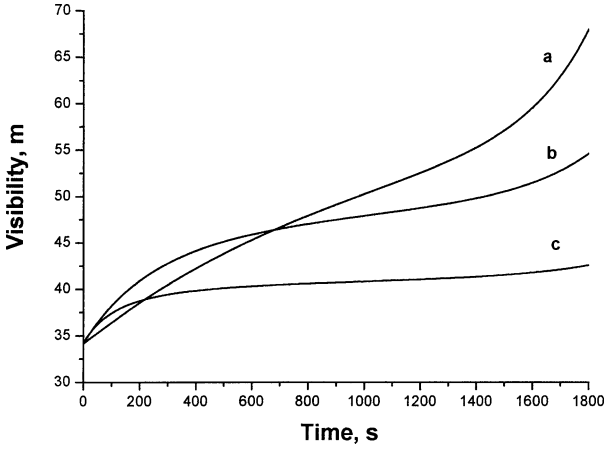

FIG. 15. Time evolution of the fog visibility for different fraction of positively charged droplets: (a) 10%, (b) 30%, and (c) 60%.

14. Curves a, b, and c show time dependencies of visibility for the fog with the DSD presented in Fig. 13, that is, when all droplets were neutral, when 30% of droplets were charged positively and another 30% of droplets were charged negatively, and when 50% of the droplets were charged positively and 50% of the droplets were charged negatively, respectively. Whereas no change in visibility of the neutral fog takes place, a significant increase in visibility of fog with charged droplets can be seen during 30 min.

In Fig. 14 one can see three stages of fog development for the case of bipolar charging. At the first stage within the first 10 s of fog evolution fast collisions of oppositely charged droplets lead to increase in visibility from 35 up to 40 m (see upper framed figure in Fig. 14) and net charge decrease as presented in the lower framed picture. These collisions shift the fog DSD toward to the region of larger droplets. Then, at the second stage of about 20-min duration, the evolution of fog is mainly governed by gravity-induced collisions (because the charge concentration decreases by one order of magnitude at the first stage). During the second stage visibility grows slowly. However, gravity collisions lead to the creation of some amount of large droplets, which later trigger the fast collision process evident at the third stage (after 20 min) of fog evolution.

To investigate the development of unipolar-charged fog, we conducted numerical simulations with 10%, 30%, and 60% of the charged droplets. The increase in visibility in these simulations is presented in Fig. 15 by curves a, b, and c, respectively. A unipolar-charged fog does not reveal these three stages of development, which are found in the case of bipolar-charged fog. This can be attributed to the absence of charged compensation. Thus, in contrast to the bipolar-charged fog, the electrostatic effects are important over the whole period of the fog evolution. Nevertheless, in the case of a unipolar-charged fog, elimination is not as efficient as in the case of bipolar charging (cf. Figs. 14 and 15).

The dependence of visibility (at $t = 30$ min) as a function of the fraction of droplets with a unipolar charge is presented in Fig. 16. One can see that there exists an optimum fraction of droplets with a unipolar charge, when visibility increases faster than for all other concentrations of charged droplets. The existence of this optimum could be explained by a simple physical reason. In a natural fog, when all droplets are neutral, gravity-induced collisions are inefficient and do not lead to the DSD development and fog elimination. In a totally charged fog (100% of charged droplets) even the gravitational collisions are drastically suppressed by the Coulomb force repulsion. Thus, between these two ineffective situations should be an optimum, which for the DSD used in our simulation occurs at 10% of unipolar-charged droplets in fog (see Fig. 16).

The last numerical experiment presented here is seed-

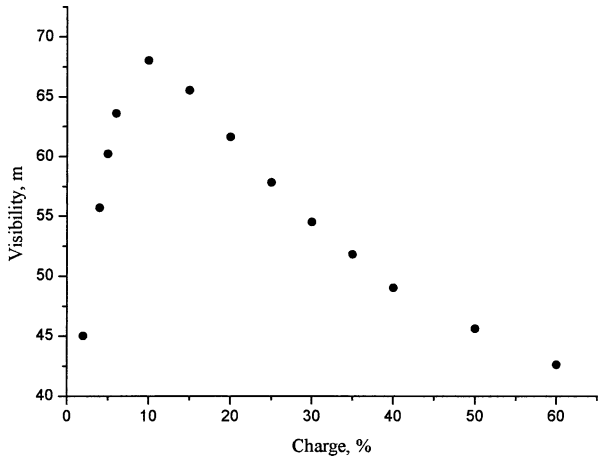

FIG. 16. Visibility (at $t = 30$ min) as a function of unipolar charge concentration.

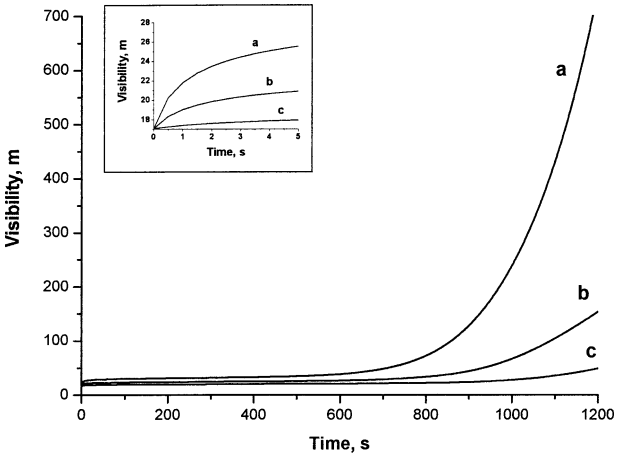

FIG. 17. Time evolution of visibility in a dense fog for different fractions of positively and negatively charged droplets: (a) 50% positive, 50% negative, (b) 30% positive, 30% negative, and (c) 10% positive, 10% negative. Framed figure shows the beginning stage of the fog evolution.

ing of a dense fog by the bipolar-charged droplets. For this purpose we used the DSD similar to that in the previous experiments (results are plotted in Fig. 14), but with doubled droplet concentration. This fog can be considered as quite dense, which is of special danger for aviation and vehicular traffic. The time dependencies of visibility for these experiments are presented in Fig. 17. One can see a paradoxical effect, namely, the dense fog, having initially a smaller visibility as compared with the less dense fog in Fig. 14, is eliminated faster and in 15 min visibility becomes larger than in the case of the less dense fog. This result could be attributed to the fact that the active coagulation stage in a dense fog in the presence of charged droplets starts earlier and runs more efficiently than in a less dense fog.

Concluding the discussion of the fog elimination process, we note that no droplets sedimentation was taken into account in the simulations. This assumption, together with the underestimation of the collision efficiencies mentioned earlier, leads to an underestimation of the fog elimination rate.

6. Conclusions

A new method of droplet collision acceleration with the purposes of rain enhancement and fog elimination is proposed. According to the method some fraction of droplets is charged and injected into clouds. It is clear that clouds and especially fogs can be seeded by charged droplets produced by droplet generators as well. To simulate the evolution of a droplet spectrum, a novel model (taking into account the electrostatic droplet interaction effects) was developed. To elaborate this model, an approximate expression for the electrostatic force has been derived. This expression was used to calculate a table of collision efficiencies for different radii and charges of colliding droplets. The table was implemented into the coagulation model using a two-dimensional mass charge grid.

It was found that the collision efficiency between charged and neutral droplets, as well as between droplets containing charges of opposite polarity, is many orders higher than in cases of the corresponding gravity-induced collisions. Thus, efficient collisions take place between cloud droplets. This significantly increases the rate of raindrop formation and decreases the concentration of small droplets (responsible for low visibility in fogs).

The results of numerical experiments show the efficiency of rain enhancement by seeding with charged droplets. A striking result of numerical experiments is the creation of precipitation in extreme continental Texas-type clouds, which do not produce warm rain under natural conditions. A significant acceleration of raindrop formation was found also in the case of the maritime droplet spectrum. This is the main result of the paper. The seeding with unipolar-charged droplets was found to be more efficient for rain enhancement.

It is shown also that seeding with charged droplets fosters fog elimination. It was found that if small fog droplets are charged, the bipolar droplet seeding is preferable for this purpose. We suppose the existence of an optimum size of droplets to be charged and injected in fogs to provide the maximum rate of fog elimination.

Practical advantages of the proposed method are the following:

1) There is very high efficiency of seeding with charged droplets for the collision rate acceleration, leading to raindrop formation in clouds and an increase in the visibility in fogs.
2) There is no necessity for a special reagent material. The ''seeding'' time with charged droplets taken from clouds (and fog) is limited by the storage of fuel in an airplane.
3) The method allows consideration of fog as a source of freshwater.
4) Seeding by charged particles leads to no pollution formation.

The results of presented numerical experiments should be tested in laboratory and field experiments.

Acknowledgments. This study has been conducted under the support of YISSUM (The Hebrew University of Jerusalem) and the Yeshua Hororwitz Association, as well as under partial support of the Israel Science Foundation (Grant 173/03) and the Israel Ministry of Science (Germany–Israel collaboration in Water Resources Grant WT 0403).

APPENDIX A

Electrostatic Force between Charged Droplets

Coulomb's law establishes that the force of interaction arising between two charged point particles obeys the law of reciprocal squares,

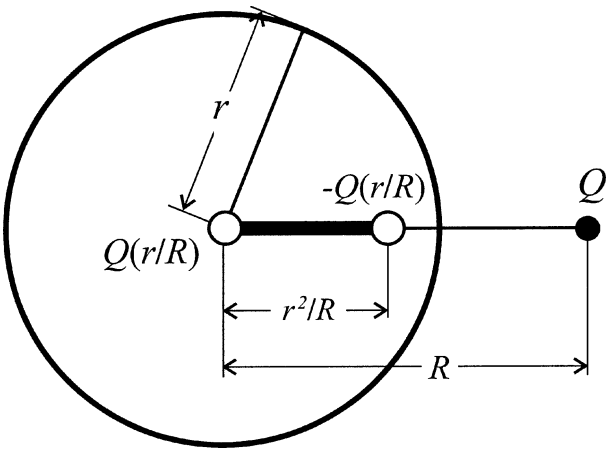

FIG. A1. A scheme illustrating a short-range electrostatic interaction arising between a large uncharged insulated conducting particle and a small point charge.

$$F = \frac{1}{4\pi\varepsilon_0}\frac{Q_1 Q_2}{R^2}, \tag{A1}$$

where Q_1 and Q_2 are the particles' charges, R is the distance between their centers, and $\varepsilon_0 = 8.854 \times 10^{-12}$ F m^{-1} is the dielectric permittivity of free space (Bleaney and Bleaney 1993, p. 2). According to this law, $F < 0$ (charges of different polarity) corresponds to attractive interaction, while $F > 0$ signifies repulsion between the particles. Equation (A1) can approximate the interaction between cloud droplets if they are situated sufficiently far away from one another.

In the case in which one small charged droplet with charge Q approaches a large uncharged insulated conductive droplet, the interaction between these droplets becomes more complicated because the charged droplet induces some imaginary charges on the surface of the large droplet. Because the large droplet is insulated, the potential on its surface should be constant. There is only one possible charge distribution that satisfies this condition. Such a distribution can be represented by two imaginary charges inside a large droplet: the first charge $Q(r/R)$ situated at the large droplet center and the second charge $-Q(r/R)$ placed on the line connecting the centers of big and small droplets at the distance r^2/R from the big droplet center, where r is the radius of big droplet (see Fig. A1). One can regard these two imaginary charges as an apparent dipole induced in the big conductive particle by the small point charge. Thus, the electrostatic force arising between these two particles is (Bleaney and Bleaney 1993)

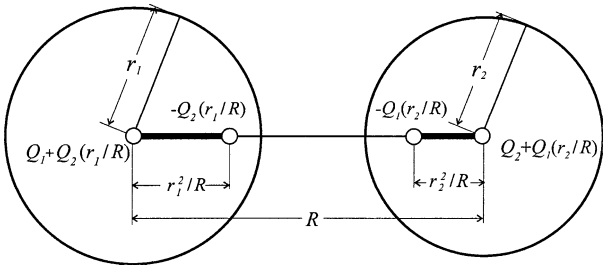

FIG. A2. A scheme illustrating an equivalent charge location for two charged insulated droplets.

$$F = \frac{Q^2}{4\pi\varepsilon_0}\left[\frac{r}{R^3} - \frac{Rr}{(R^2 - r^2)^2}\right], \tag{A2}$$

which represents the interaction of the point charge corresponding to the small droplet and the induced dipole moment of the large droplet.

If the large droplet has a nonzero charge Q_b, then the charge $Q(r/R)$ at its center should be substituted by $Q_b + Q(r/R)$, and the resulting force is

$$F = \frac{Q^2}{4\pi\varepsilon_0}\left[\frac{r}{R^3} - \frac{Rr}{(R^2 - r^2)^2}\right] + \frac{Q_b Q}{4\pi\varepsilon_0 R^2}, \tag{A3}$$

where the first term on right-hand side of (A3) once again represents the interaction between charge Q and the induced dipole moment, and the second term describes Coulomb force's interaction between the droplets.

In the case of interaction between two conductive insulated charged droplets with charges Q_1 and Q_2 and radii r_1 and r_2, respectively (Fig. A2), the approximated expression for the force of interaction can be derived. We assume that for both droplets the approximated distribution of induced charges is the same as in the case in which the counterpart droplet is regarded as a point charge. Thus, the charge Q_1 induces imaginary charges $-Q_1(r_2/R)$ and $Q_1(r_2/R)$ inside the second droplet and vice versa. Then, the approximated force of interaction between two charged droplets can be represented as the sum of three parts: the Coulomb force's interaction between the droplets, the interaction between droplet charges and the induced dipole moments on counterpart droplets, and the interaction between the induced dipole moments:

$$F_{\text{el}} = \frac{Q_1 Q_2}{4\pi\varepsilon_0 R^2} + \frac{1}{4\pi\varepsilon_0}\left\{Q_1^2 r_2\left[\frac{1}{R^3} - \frac{R}{(R^2 - r_2^2)^2}\right] + Q_2^2 r_1\left[\frac{1}{R^2} - \frac{R}{(R^2 - r_1^2)^2}\right] + Q_1 Q_2 r_1 r_2\left[\frac{1}{R^4} + \frac{1}{(R^2 - r_1^2 - r_2^2)^2} - \frac{1}{(R^2 - r_1^2)^2} - \frac{1}{(R^2 - r_2^2)^2}\right]\right\}. \tag{A4}$$

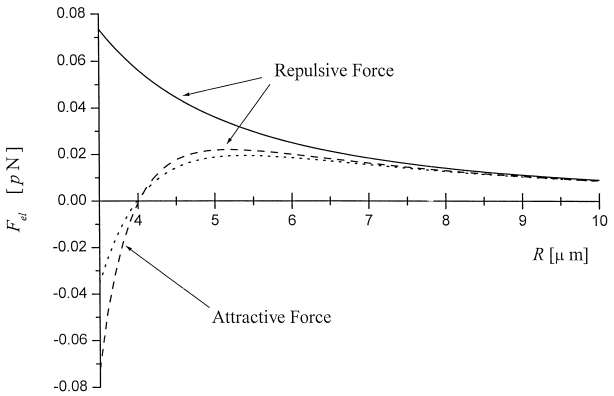

FIG. A3. Comparison between the electrical forces caused by Coulomb's law (solid line) and the electrostatic interaction force F_{el} arising between two small cloud droplets of equal charge $q_1 = q_2 = 1(10^{-17})$ C, but with slightly different radii $r_1 = 1$ μm, $r_2 = 2.5$ μm (dash–dotted line). Dashed line denotes exact solution for the attraction force.

Equation (A4) provides the Coulomb limit when the distance between the droplets R becomes much bigger than the particles radii r_1 and r_2.

Figure A3 presents a comparison of electrostatic forces calculated using the approximation expression (A4) and the exact solution of the problem (Smythe 1950, 118–121) arising between two small cloud droplets of equal charges $q_1 = q_2 = 1 \times 10^{-17}$ C, but with slightly different radii $r_1 = 1$ μm and $r_2 = 2.5$ μm. The repulsion force caused by Coulomb's law is denote by a solid line, while the total electrostatic interaction force F_{el} arising between these droplets is denoted by a dash–dotted line. A dashed line denotes the exact solution. Despite the fact that (A4) is an approximate solution, it reproduces fine effects, such as the attraction arising between droplets charged with similar polarity at small separation distances. One can see a good qualitative and even quantitative agreement of the exact and approximated solutions at separation distances exceeding 4 μm. A transition to the Coulomb limit is seen with the increase in the separation distance between droplets. One can see that at small separation distances the approximate solution (A4) tends to underestimate the attraction force.

APPENDIX B

The Maximum Charge of a Cloud Droplet

Theoretically, an insulated droplet in a vacuum can be loaded with a charge of an arbitrary large magnitude. However, a cloud droplet situated in the air cannot be loaded with a charge exceeding a certain maximum value $q_{\max}$, which is determined by the air breakdown voltage $U_b \sim 3 \times 10^6$ V m^{-1} (Meek and Craggs 1953).

The voltage in the vicinity of a charged spherical particle is given by the well-known formula $U = q/4\pi\varepsilon_0 r^2$ (Bleaney and Bleaney 1993). The magnitude of the maximum possible charge of a cloud droplet can be evaluated by using the condition $U = U_b$, which gives

$$q_{\max} = 4\pi U_b \varepsilon_0 r^2. \quad \text{(B1)}$$

If the charge of a cloud droplet is higher than $q_{\max}$ then the voltage in the vicinity of this charged droplet surface exceeds U_b value and a corona discharge immediately appears. This fast process reduces the charge of the droplet to the value $q_{\max}$, at which the corona discharge stops.

REFERENCES

Batygin, V. V., and I. N. Toptygin, 1978: *Problems in Electrodynamics.* Academic Press, 574 pp.

Berry, E. X., and R. L. Reinhardt, 1974: An analysis of cloud droplet growth by collection: Part I. Double distributions. *J. Atmos. Sci.*, **31,** 1814–1824.

Bigg, E. K., 1997: An independent evaluation of a South African hygroscopic cloud seeding experiment, 1991–1995. *Atmos. Res.*, **43,** 111–127.

Bleaney, B. I., and B. Bleaney, 1993: *Electricity and Magnetism,* Vol. 1. Oxford University Press, 676 pp.

Bleck, R., 1970: A fast, approximative method for integrating the stochastic coalescence equation. *J. Geophys. Res.*, **75,** 5165–5171.

Bott, A., 1998: A flux method for the numerical solution of the stochastic collection equation. *J. Atmos. Sci.*, **55,** 2284–2293.

Bruintjes, T. R., 1999: A review of cloud seeding experiments to enhance precipitation and some new prospects. *Bull. Amer. Meteor. Soc.*, **80,** 805–820.

DuBard, J. L., J. R. McDonald, and L. E. Sparks, 1983: First measurement of aerosol particle charging by free electrons—A preliminary report. *J. Aerosol Sci.*, **14,** 5–10.

Grover, S. N., and K. V. Beard, 1975: A numerical determination of the efficiency with which electrically charged cloud drops and small raindrops collide with electrically charged spherical particles of various densities. *J. Atmos. Sci.*, **32,** 2156–2165.

Khain, A. P., M. Ovtchinnikov, M. Pinsky, A. Pokrovsky, and H. Krugliak, 2000: Notes on the state-of-the-art numerical modeling of cloud microphysics. *Atmos. Res.*, **55,** 159–224.

——, D. Rosenfeld, and A. Pokrovsky, 2001: Simulation of deep convective clouds with sustained supercooled liquid water down to −37.5°C using a spectral microphysics model. *Geophys. Res. Lett.*, **28,** doi:10.1029/2000GL012662.

Kim, S., and S. J. Karrila, 1991: *Microhydrodynamics Principles and Selected Applications.* Butterworth-Heinmann, 507 pp.

Kovetz, A., and B. Olund, 1969: The effect of coalescence and condensation on rain formation in a cloud of finite vertical extent. *J. Atmos. Sci.*, **26,** 1060–1065.

Kunkel, B. A., 1984: Parameterization of droplet terminal velocity and extinction coefficient in fog models. *J. Climate Appl. Meteor.*, **23,** 34–41.

Langmuir, I., 1948: The production of rain by a chain reaction in cumulus clouds at temperature above freezing. *J. Meteor.*, **5,** 175–192.

Lin, C. L., and S. C. Lee, 1975: Collision efficiency of water drops in the atmosphere. *J. Atmos. Sci.*, **32,** 1412–1418.

Mather, G. K., M. J. Dixon, and J. M. de Jager, 1996: Assessing the potential for rain augmentation—The Nelspruit randomized convective cloud seeding experiment. *J. Appl. Meteor.*, **35,** 1465–1482.

——, D. E. Terblanche, F. E. Steffens, and L. Fletcher, 1997: Results of the South African cloud-seeding experiments using hygroscopic flares. *J. Appl. Meteor.*, **36,** 1433–1447.

Meek, J. M., and J. D. Craggs, 1953: *Electrical Breakdown of Gases.* Clarendon Press, 507 pp.

Pinsky, M., and A. P. Khain, 2002: Effects of in-cloud nucleation and turbulence on droplet spectrum formation in cumulus clouds. *Quart. J. Roy. Meteor. Soc.*, **128,** 1–33.

——, ——, and M. Shapiro, 1999: Collisions of small drops in a turbulent flow. Part I: Collision efficiency. Problem formulation and preliminary results. *J. Atmos. Sci.,* **56,** 2585–2600.

——, ——, and ——, 2001: Collision efficiency of drops in a wide range of Reynolds numbers: Effects of pressure on spectrum evolution. *J. Atmos. Sci.,* **58,** 742–764.

Press, W. H., S. A. Tenkolsky, W. T. Vetterling, and B. P. Flannery, 1992: *Numerical Recipes in FORTRAN*. Cambridge Press, 963 pp.

Pruppacher, H. R., and J. D. Klett, 1997: *Microphysics of Clouds and Precipitation.* Kluwer Academic Publishers, 954 pp.

Reisin, T., S. Tzivion, and Z. Levin, 1996: Seeding convective clouds with ice nuclei or hygroscopic particles: A numerical study using a model with detailed microphysics. *J. Appl. Meteor.,* **35,** 1416–1434.

Roach, W. T., R. Brown, S. J. Caughey, J. A. Garland, and C. J. Readings, 1976: The physics of radiation fog: I—A field study. *Quart. J. Roy. Meteor. Soc.*, **102,** 313–333.

Rosenfeld, D., and G. Gutman, 1994: Retrieving microphysical properties near the tops of potential rain clouds by multispectral analysis of AVHRR data. *Atmos. Res.,* **34,** 259–283.

——, and W. L. Woodley, 2000: Convective clouds with sustained highly supercooled liquid water down to −37.5°C. *Nature,* **405,** 440–442.

Schlamp, R. J., S. N. Grover, H. R. Pruppacher, and A. E. Hamielec, 1976: A numerical investigation of the effect of electric charges and vertical external electric fields on the collision efficiency of cloud drops. *J. Atmos. Sci.,* **33,** 1747–1755.

Seeßelberg, M., T. Trautmann, and M. Thorn, 1996: Stochastic simulations as a benchmark for mathematical methods solving the coalescence equation. *Atmos. Res.,* **40,** 33–48.

Segal, Y., A. Khain, M. Pinsky, and D. Rosenfeld, 2004: Effects of hygroscopic seeding on raindrop formation as seen from simulations using a 2000-bin spectral cloud parcel model. *Atmos. Res.,* **71,** 3–34.

Shafrir, U., and T. Gal-Chen, 1971: A numerical study of collision efficiencies and coalescence parameters for droplet pairs with radii up to 300 microns. *J. Atmos. Sci.,* **28,** 741–751.

Silverman, B. A., and W. Sukarnjanaset, 2000: Results of the Thailand warm-cloud hygroscopic particle seeding experiment. *J. Appl. Meteor.,* **39,** 1160–1175.

Smythe, W. R., 1950: *Static and Dynamic Electricity*. 2d ed. McGraw-Hill, 240 pp.

Tinsley, B. A., R. P. Rohrbauch, M. Hei, and K. V. Beard, 2000: Effects of image charges on the scavenging of aerosol particles by cloud droplets and on droplet charging and possible ice nucleation processes. *J. Atmos. Sci.,* **57,** 2118–2134.

——, ——, and ——, 2001: Electroscavenging in clouds with broad droplet size distributions and weak electrification. *Atmos. Res.*, **59–60,** 115–135.

Tzivion, S., G. Feingold, and Z. Levin, 1987: An efficient numerical solution to the stochastic collection equation. *J. Atmos. Sci.,* **44,** 3139–3149.

Wang, P. K., S. N. Grover, and H. R. Pruppacher, 1978: On the effects of electric charge on the scavenging of aerosol particles by clouds and small raindrops. *J. Atmos. Sci.,* **35,** 1735–1743.

Woodley, W. L., and D. Rosenfeld, 1999: Comparison of radar-derived properties of Texas clouds receiving one of three treatments: AgI ejectable flares or hygroscopic flares or no seeding. *J. Wea. Modif.,* **31,** 29–41.

Yin, Y., Z. Levin, T. G. Reisin, and S. Tzivion, 2000: Seeding convective clouds with hygoscopic flares. Numerical simulations using a cloud model with detailed microphysics. *J. Appl. Meteor.,* **39,** 1460–1472.

——, ——, ——, and ——, 2001: On the response of radar-derived properties to hygroscopic flare seeding. *J. Appl. Meteor.,* **40,** 1654–1661.

Zuev, V. E., 1974: Propagation of visible and infrared radiation in the atmosphere (translated from Russian ''Sovetskoe Radio'' Moscow, 1970). Israel Program for Soviet Translations.